Electronic Supplementary Material (ESI) for Dalton Transactions.
This journal is © The Royal Society of Chemistry 2023

Facile Surface Defect Engineering on Perovskite Oxide for Enhanced OER Performance

Shu-Fang Li,*[ab] Jie Zheng,[a] Liang Hu,[a] Yao Ma,[a] and Dong Yan*[ab]

[a] Key Laboratory of Functional Molecular Solids, Ministry of Education, College of Chemistry and Materials Science, Anhui Normal University

Wuhu, Anhui 241002, P. R. China

E-mail: lishufang@mail.ahnu.edu.cn; yandong8@ahnu.edu.cn

[b] State Key Laboratory of Structural Chemistry, Fujian Institute of Research on the Structure of Matter, Chinese Academy of Sciences

Fuzhou, Fujian 350002, P. R. China

Supporting Information

Section S1. Experimental section

Table S1. Comparison of OER activities of our catalyst with those of previously reported catalysts.

Table S2. Relative oxygen concentration of SCFO and SCFO-24 catalysts.

Figure S1. SEM images of (a) SCFO, (b) SCFO-3, (c) SCFO-6, (d) SCFO-12, (e) SCFO-24, and (f) SCFO-28.

Figure S2. (a) SEM image and (b) N_2 adsorption/desorption isotherms and the corresponding surface area of SCFO-28.

Figure S3. SEM-EDS mapping for SCFO and SCFO-*x*.

Figure S4. (a-b) TEM image of SCFO, (c) lattice diffraction pattern of SCFO, (d-f) TEM images of SCFO-24.

Figure S5. CVs of SCFO and SCFO-*x* at different scan rates (20, 40, 60, 80, 100 mV/s) under nonfaradaic region in O_2-saturated 1.0M KOH solution.

Figure S6. ECSA-corrected LSV curves of SCFO and SCFO-*x*.

Figure S7. Chronopotentiometry curve of SCFO-24 for 20 h.

Figure S8. XPS spectra of (a) Co 2*p* and (b) Fe 2*p* of SCFO and SCFO-24 catalysis.

Figure S9. TGA curve of SCFO-24.

Section S1. Experimental section

Chemicals.

All chemicals were of analytical grade and used without further purification. $Sr(NO_3)_2$, $Co(NO_3)_2 \cdot 6H_2O$, $Fe(NO_3)_3 \cdot 9H_2O$, citric acid were purchased from Macklin Chemical Reagent Co., Ltd. KOH, ethylene glycol ($C_2H_4O_2H_2$), acid (HNO_3), and absolute alcohol were purchased from Sinopharm Chemical Reagent Co., Ltd. Nafion were obtained from Alfa Aesar.

Characterization of SCFO and SCFO-*x*.

Powder X-ray diffraction (XRD) spectra of SCFO and SCFO-*x* were obtained with a D8 powder XRD system (Bruker) using Cu Kα (λ = 1.5418 Å) as the X-ray source. Symmetric $\theta/2\theta$ measurements were performed in the 2θ range of 10−80° with at the scan rate 1° per minute. The microscopic morphology of the electrocatalyst and energy-dispersive X-ray spectroscopy (EDS) data were measured using a field emission scanning electron microscope (SEM, FEI Inspect F50). The transmission electron microscopy (TEM, FEI Tecnai F30 Twin) was used to characterize the interplanar spacings and the microscopic structure. The surface valence of elements was investigated from X-ray photoelectron spectra (XPS, Thermo Fisher, Escalab 250Xi). Binding energy of *C*1s, located at 284.8 eV, was taken as the reference standard. The specific surface area of as-prepared catalyst samples was measured by the low-temperature nitrogen adsorption and desorption (Quantachrome Instruments) and calculated according to Brunauer-Emmett-Teller (BET) method. The molar ratio of the sample elements was determined by inductively coupled plasma atomic emission spectrometry (ICP).

Electrochemical Performances of SCFO and SCFO-*x*.

Electrochemical measurements were performed on an electrochemical workstation (CHI 760E) in a standard three-electrode system. A graphite rod and an Hg/HgO electrode were used as the counter and the reference electrodes, respectively. All tests were measured in a solution of 1.0 M KOH (pH = 14). The working electrodes were prepared by loading the catalyst inks onto glassy carbon. The catalyst inks were

prepared using a typical method as follows: 10 mg of materials were dispersed in a mixed solution containing 1 mL of ethanol and 70 μL of a Nafion solution (5 wt %, Sigma-Aldrich). The mixture was then sonicated for 30 min to form a homogeneous ink. Then, 3 μL as-prepared ink was dropped and then dried on a mirror-polished glassy carbon electrode (GCE), giving rise to a catalyst mass loading of 0.397 mg cm^{-2}.

The O_2-saturated 1.0 M KOH solution was used as an electrolyte. During the test, magnetic stirring (400 $r \cdot min^{-1}$) was used to remove the formed O_2 bubbles on the working electrode. Before the test, the cyclic voltammetry (CV) activation was performed from 1.03 to 1.13 V (vs reversible hydrogen electrode, RHE) at a scanning rate of 10 mVs^{-1} until the material reached a stable state. All potentials were converted to a RHE scale through the following equation: E (*vs*. RHE) = E (*vs*. Hg/HgO) + 0.098 + 0.0591 × pH. Linear sweep voltammetry (LSV) was tested at a scan rate of 5 mVs^{-1} and without internal resistance (*i*R) compensation. The Tafel slopes of the catalysts were obtained to study the electrocatalytic kinetics of the OER through the equation $\eta = a + b\log j$. In which j, a, b, and η represented the current density, fitting parameter, Tafel slope, and overpotential respectively. The electrochemical double-layer capacitance (C_{dl}) can be obtained by measuring the current density at different scan rates (20, 40, 60, 80, 100 mVs^{-1}) on the non-Faraday region by cyclic voltammetry. Then, the plots of half of the capacitive current (ΔJ, $(J_{anodic} - J_{cathodic})/2$) against the scan rate were plotted, and the slope was calculated and defined as the double-layer capacitance (C_{dl}). Therefore, the current was expected to be linearly proportional to the active surface area owing to the charging of the double layer. Electrochemical impedance spectroscopy (EIS) was recorded at open circuit potential with an amplitude of 10 mV and the frequency from 10^6 to 10^{-2} Hz. Chronopotentiometry measurement was used to evaluate the stability of the catalysts a constant current density of 10 mA cm^{-2}.

Table S1. Comparison of OER activities of our catalyst with those of previously reported catalysts.

Catalysts	Electrolyte	overpotential @10 mA cm^{-2} (mV)	Tafel (mV dec^{-1})	Reference
SCFO-24	1M KOH	300	59.62	This work
$Sr_6(Co_{0.8}Fe_{0.2})_5O_{15}$	1M KOH	318	54	[1]
$La_{0.9}Sn_{0.1}NiO_{3-\delta}$	1M KOH	318	74	[2]
$LaFe_{0.2}Ni_{0.8}O_3$	1M KOH	302	50	[3]
$La_{0.6}Sr_{0.4}Co_{0.8}Fe_{0.2}O_3$	1M KOH	353	63	[4]
$La_{0.6}Sr_{0.4}Co_{0.2}Fe_{0.2}Mn_{0.2}Ni_{0.2}Mg_{0.2}O_3$	1M KOH	320	45	[5]
$KNi_{0.8}Co_{0.2}F_3$	1M KOH	310	49	[6]
$LaCo_{0.8}V_{0.2}O_3$	1M KOH	306	40	[7]
$GdCoO_3$	1M KOH	320	53.5	[8]

Table S2. Relative oxygen concentration of SCFO and SCFO-24 catalysts.

	Lattice O	O_2^{2-}/O^-	Surface OH^-/O_2	Surface H_2O
SCFO	0.069	0.118	0.694	0.118
SCFO-24	0.047	0.442	0.274	0.236

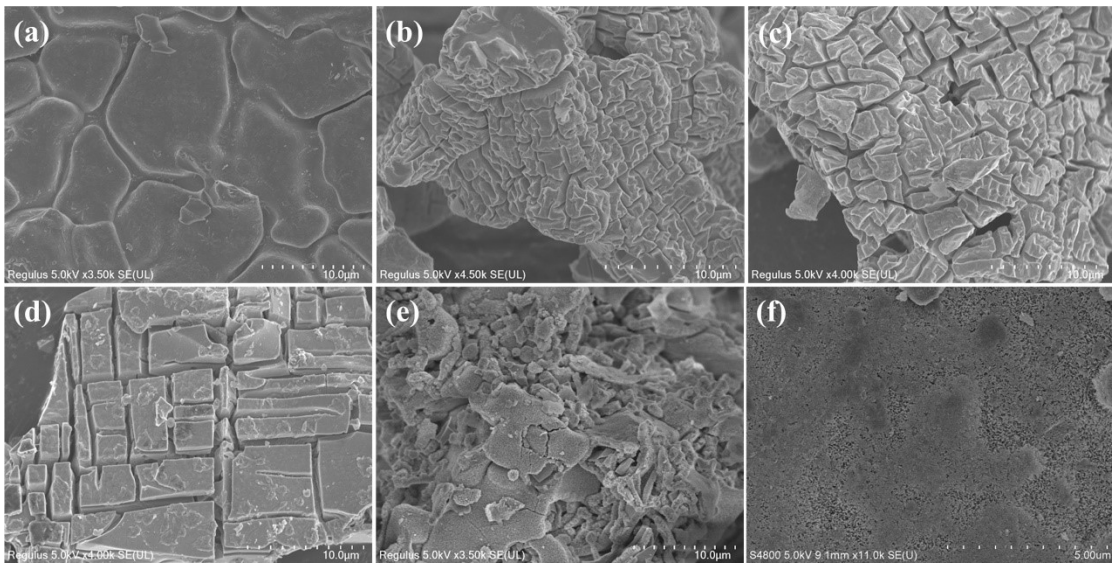

Figure S1. SEM images of (a) SCFO, (b) SCFO-3, (c) SCFO-6, (d) SCFO-12, (e) SCFO-24, and (f) SCFO-28.

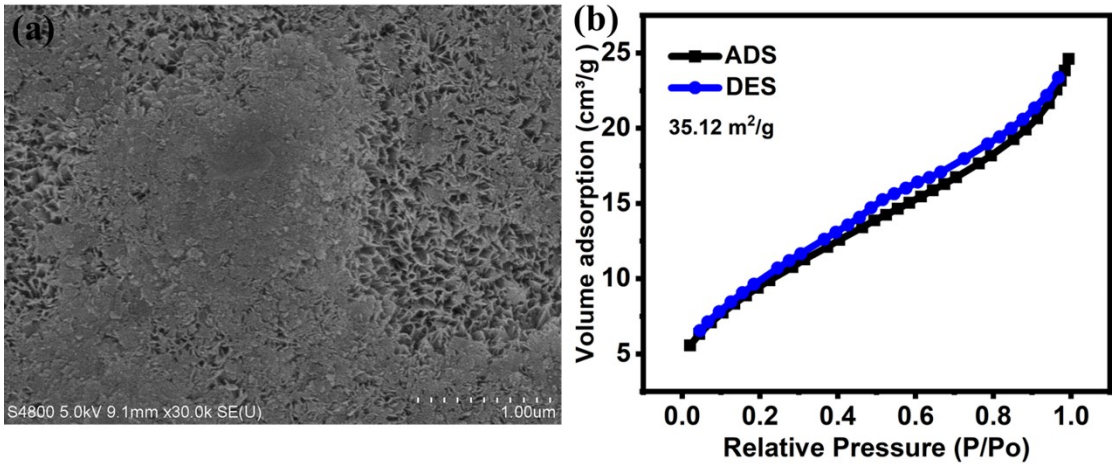

Figure S2. (a) SEM image and (b) N_2 adsorption/desorption isotherms and the corresponding surface area of SCFO-28.

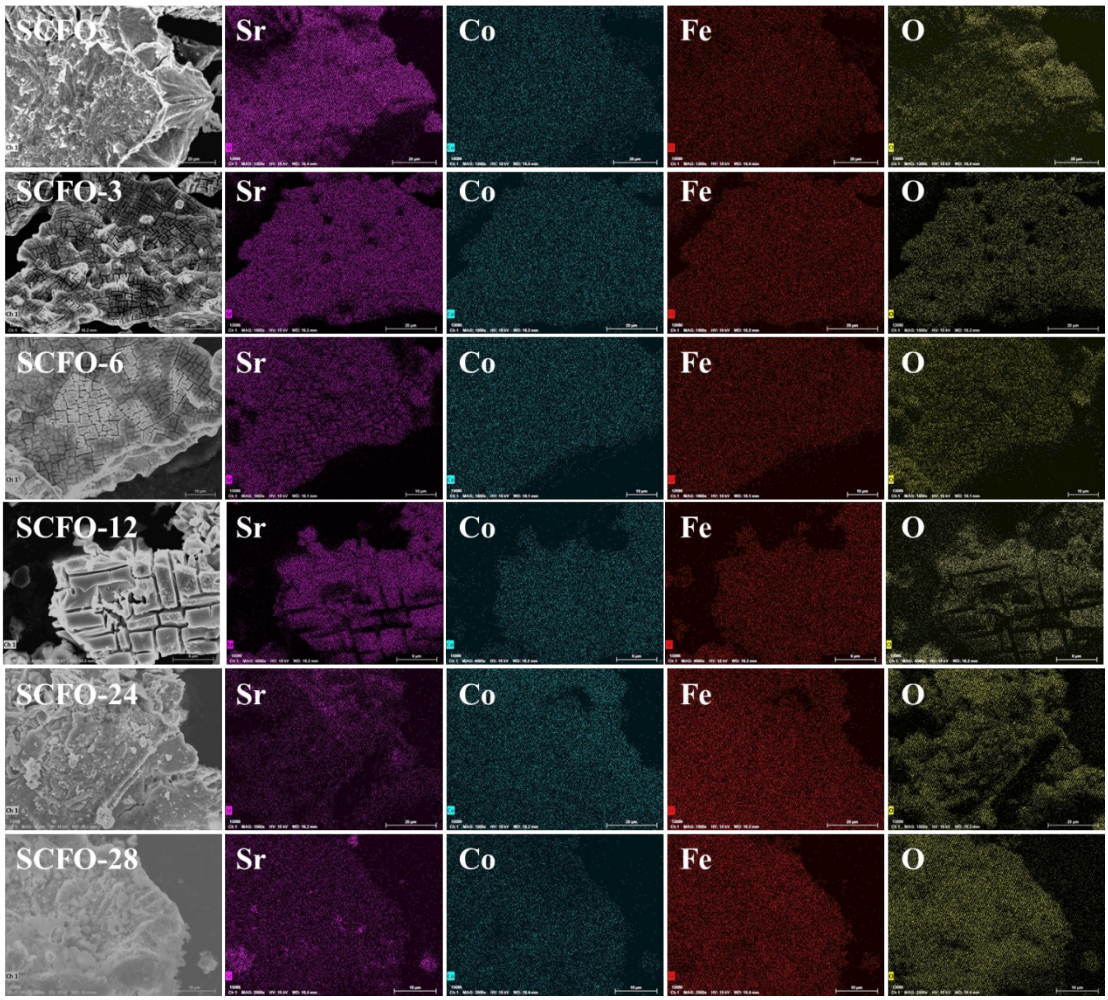

Figure S3. SEM-EDS mapping for SCFO and SCFO-*x*.

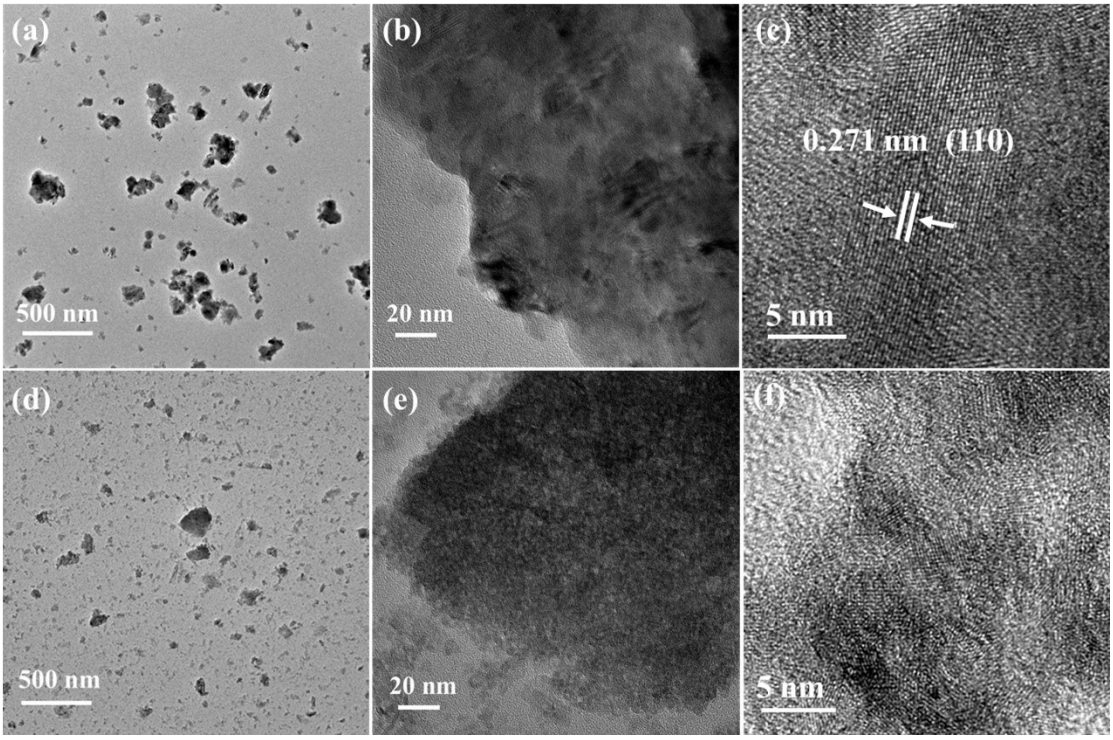

Figure S4. (a-b) TEM image of SCFO, (c) lattice diffraction pattern of SCFO, (d-f) TEM images of SCFO-24.

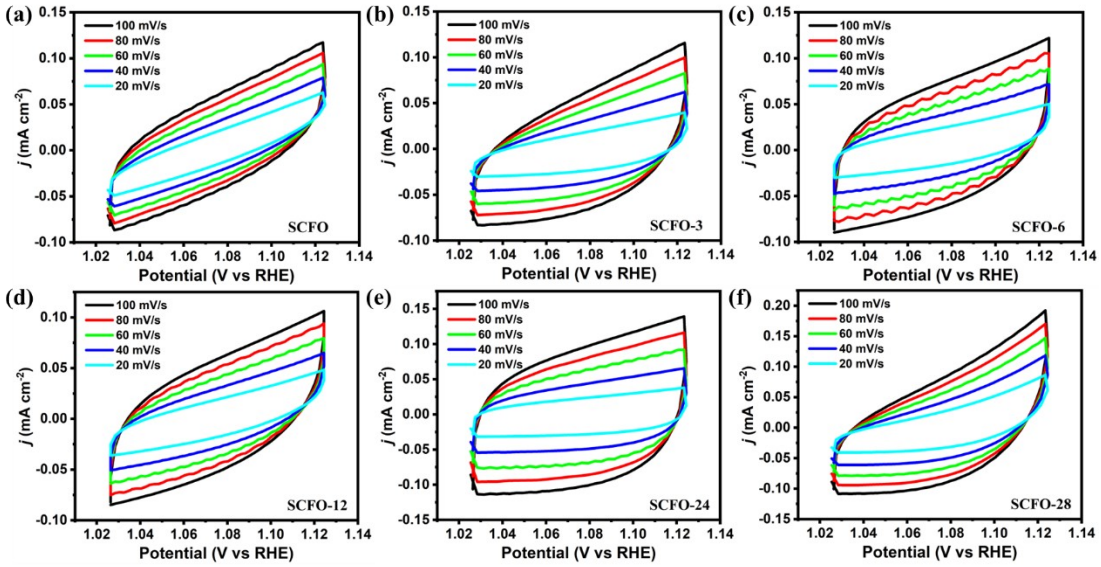

Figure S5. CVs of SCFO and SCFO-*x* at different scan rates (20, 40, 60, 80, 100 mV/s) under nonfaradaic region in O_2-saturated 1.0 M KOH solution.

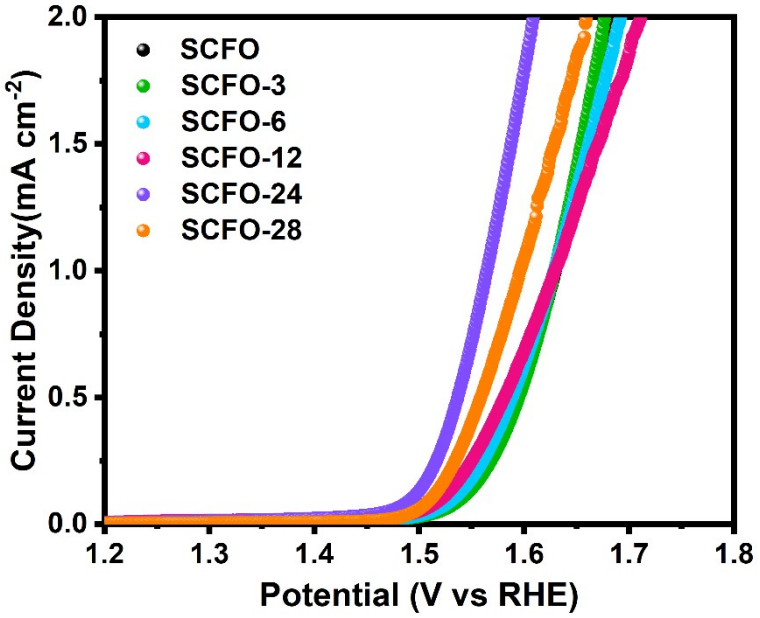

Figure S6. ECSA-corrected LSV curves of SCFO and SCFO-*x*.

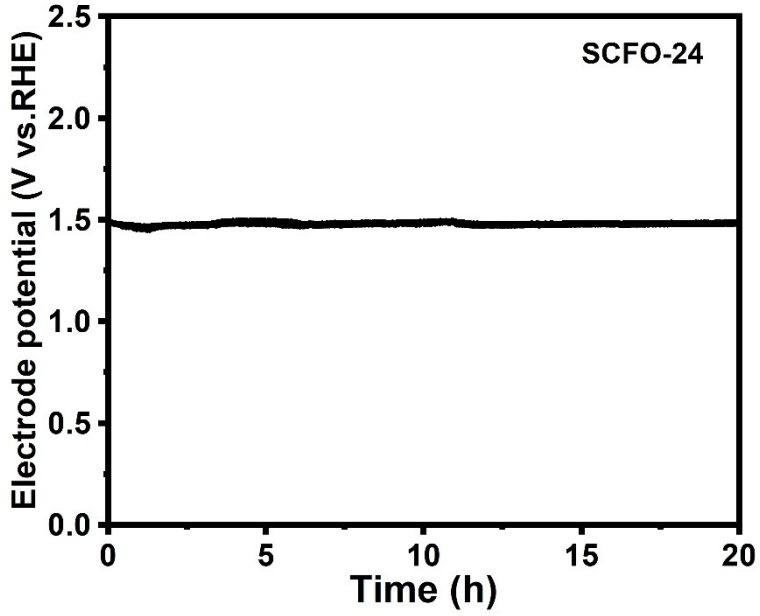

Figure S7. Chronopotentiometry curve of SCFO-24 for 20 h.

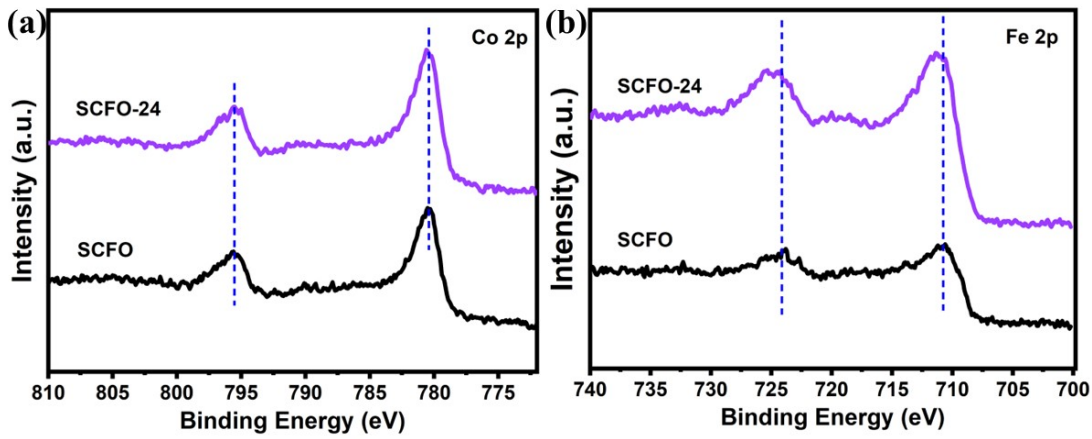

Figure S8. XPS spectra of (a) Co 2*p* and (b) Fe 2*p* of SCFO and SCFO-24 catalysis.

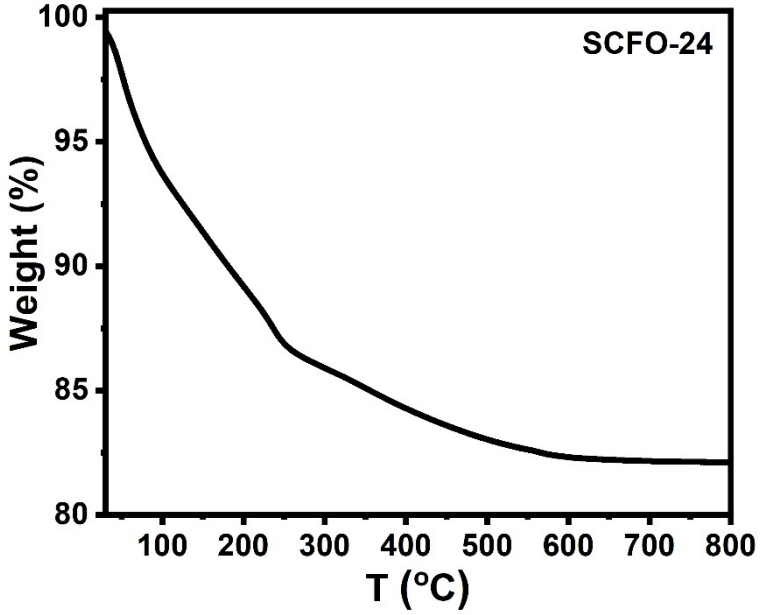

Figure S9. TGA curve of SCFO-24.

Reference

1. L. Wei, J. Hu, H. Liu, W. Zhang, H. Zheng, S. Wu and K. Tang, Hexagonal perovskite $Sr_6(Co_{0.8}Fe_{0.2})_5O_{15}$ as an efficient electrocatalyst towards the oxygen evolution reaction, *Dalton Trans.*, 2022, **51**, 7100-7108.

2. C. Liu, D. Ji, H. Shi, Z. Wu, H. Huang, Z. Kang and Z. Chen, An A-site management and oxygen-deficient regulation strategy with a perovskite oxide electrocatalyst for the oxygen evolution reaction, *J. Mater. Chem. A*, 2022, **10**, 1336-1342.

3. H. Wang, J. Wang, Y. Pi, Q. Shao, Y. Tan and X. Huang, Double Perovskite $LaFe_xNi_{1-x}O_3$ nanorods enable efficient oxygen evolution electrocatalysis, *Angew. Chem. Int. Ed.*, 2019, **131**, 2338-2342.

4. L. Zhang, H. Zhu, J. Hao, C. Wang, Y. Wen, H. Li, S. Lu, F. Duan and M. Du, Integrating the cationic engineering and hollow structure engineering into perovskites oxides for efficient and stable electrocatalytic oxygen evolution, *Electrochim. Acta*, 2019, **327**, 135033.

5. L. Tang, Y. Yang, H. Guo, Y. Wang, M. Wang, Z. Liu, G. Yang, X. Fu, Y. Luo and C. Jiang, High Configuration Entropy Activated Lattice Oxygen for O_2 Formation on Perovskite Electrocatalyst, *Adv. Funct. Mater.*, 2022, **32**, 2112157.

6. S. Guddehalli Chandrappa, P. Moni, D. Chen, G. Karkera, K. R. Prakasha, R. A. Caruso and A. S. Prakash, Fluoride Perovskite ($KNi_xCo_{1-x}F_3$) Oxygen-Evolution Electrocatalyst with Highly Polarized Electronic Configuration, *ACS Appl. Energ. Mater.*, 2021, **4**, 13425-13430.

7. Y. Sun, Z. Zhao, S. Wu, W. Li, B. Wu, G. Liu, G. Chen, B. Xu, B. Kang and Y. Li, Engineering of the d-Band Center of Perovskite Cobaltite for Enhanced Electrocatalytic Oxygen Evolution, *ChemSusChem.*, 2020, **13**, 2671-2676.

8. E. Nandhakumar, P. Selvakumar, A. Sasikumar, E. Vivek and R. Kamatchi, Facile eco-friendly synthesis of rare-earth cobaltite-based perovskite nanostructures as electrocatalysts for oxygen evolution reaction, *Mater. Lett.*, 2022, **315**, 132002.